IVYSPRING INTERNATIONAL PUBLISHER

Theranostics

2019; 9(5): 1474-1489. doi: 10.7150/thno.29255

Research Paper

Molecular Imaging of Factor XIII Activity for the Early Detection of Mouse Coronary Microvascular Disease

Zhen W. Zhuang[1,2,3]✉, Yang Huang[3], Rong Ju[4], Mark W. Maxfield[5], Yongming Ren[3], Xiangning Wang[1,2], Xinlu Wang[1,2], Mitchel R. Stacy[1,2], John Hwa[1,3]

1. Section of Cardiovascular Medicine, Yale University School of Medicine, New Haven, CT, USA.
2. Yale Translational Research Imaging Center, Dept. of Internal Medicine.
3. Yale Cardiovascular Research Center, Dept. of Internal Medicine, New Haven, CT 06510-3221, USA.
4. State key laboratory of Ophthalmology, Zhongshan Ophthalmic Center, Sun Yat-sen University, Guangzhou 510060, China.
5. Dept. of Surgery, Yale University School of Medicine, New Haven, CT, USA.

✉ Corresponding author: Zhen W. Zhuang, MD, Section of Cardiovascular Medicine, Yale University School of Medicine, 375 Congress Ave, LSOG 120C, New Haven, CT 06510. Tel: 203-231-9084; Fax: 203-737-6236; e-mail: zwz2@connect.yale.edu

© Ivyspring International Publisher. This is an open access article distributed under the terms of the Creative Commons Attribution (CC BY-NC) license (https://creativecommons.org/licenses/by-nc/4.0/). See http://ivyspring.com/terms for full terms and conditions.

Received: 2018.08.15; Accepted: 2018.11.14; Published: 2019.02.20

Abstract

Coronary microvascular disease (MVD) remains a major clinical problem due to limited mechanistic understanding and a challenging diagnosis. In the present study we evaluated the utility of targeted imaging of active factor XIII (FXIII) for detection of coronary MVD associated with thrombus. We hypothesized that a high specificity and sensitivity FXIII targeted radiolabeled probe can serve as a biomarker for cross-linked thrombi in the microvasculature, and thus an indicator for underlying coronary MVD. To evaluate this approach, a coronary MVD model was established for local induction of singlet oxygen and reactive oxygen species (ROS) via a photochemical reaction (PCR).

Methods: PCR was used to induce endothelial injury and microthrombi via focal over-production of ROS only in the coronary microvasculature. Oxidative stress was initially evaluated in primary coronary endothelial cells to optimize parameters of PCR, which were then translated to *in vivo* experiments. To develop the coronary MVD model, 64 mice were assigned to one of four groups after thoracotomy: 1) sham control; 2) rose bengal; 3) green light; or 4) their combination. Following interventions, the mice underwent transmission electron microscopy, fluorescent myocardial perfusion, coronary angiography, and immunohistochemical staining. Echocardiography (n = 12) and gene expression (n = 10) studies were also performed after MVD induction to monitor serial changes in cardiac function and explore possible mechanisms. To diagnose early onset MVD, FXIII radioactivity was assessed in 104 mice using *ex vivo* gamma well counting (GWC) and in 14 mice using *in vivo* serial single photon emission computed tomography / computed tomography (SPECT/CT) imaging of a FXIII targeted technetium-labeled probe (^{99m}Tc-NC100668).

Results: *In vitro* experiments demonstrated that photosensitizer concentration and light illumination time were critical parameters for PCR. *In vivo* experiments demonstrated manifestations of clinical MVD, including endothelial damage, a "no flow zone," arteriole rarefaction with patent epicardial coronary arteries, infiltration of inflammatory cells in the PCR-treated region, and preserved cardiac function. Gene expression also demonstrated a pro-thrombotic and impaired fibrinolytic status. In the early stages of MVD, enhanced FXIII activity was confirmed within the MVD region using GWC and *in vivo* SPECT/CT imaging.

Conclusion: Our results demonstrate that molecular imaging of FXIII activity may allow for early detection of coronary MVD associated with thrombus, in a novel pre-clinical model.

Key words: coronary microvascular disease, factor XIII, photochemical reaction, micro-computed tomography, single photon emission computed tomography

Introduction

Approximately eight million Americans visit the emergency department annually complaining of chest pain; however, up to 70% of these patients are ultimately discharged with a diagnosis of unexplained chest pain (UCP) *(1)*. Coronary microvascular disease (MVD) is highly prevalent in patients with UCP, and

particularly prevalent in pre-menopausal women (*2-4*). In addition to an increased risk of major adverse cardiovascular events (*5, 6*), recurrent symptoms, repeat catheterizations/hospitalizations, and anti-angina or anti-oxidant treatments can negatively impact quality of life while also dramatically increasing economic burden *(2)*.

Endothelial dysfunction at the early stages and arteriole medial hyperplasia at the late stages are thought to contribute to the development of angina in patients with coronary MVD *(7)*. Such changes may be directly related to local increases in oxidative stress, which is commonly associated with cardiovascular risk factors (*8-11*). Reactive oxygen species (ROS) can be generated by aerobic cells during reduction of molecular oxygen by enzymatic reactions, the mitochondrial electron transport chain, and autoxidation of diverse substances (*12*). The mitochondria represents a major intracellular source of ROS (*13, 14*) and may mediate cellular oxidative stress, thereby resulting in subsequent cell damage and apoptosis *(15)*. Additionally, endothelial dysfunction may trigger platelet activation and initiate the plasma coagulation system, thereby contributing to focal hemostasis with microthrombi containing platelets and fibrin *(16)*. Soluble fibrin monomers cross-link to form insoluble fibrin polymers, in which active factor XIII (FXIII) plays a critical role. Improved understanding of the potential contribution of FXIII and time course of ROS production in pathological mechanisms of coronary MVD could greatly facilitate the development of strategies for early MVD diagnosis.

Clinically, coronary MVD can be diagnosed by both stress cardiac magnetic resonance (CMR) (*17*) and single-photon emission computed tomography (SPECT) (*18*) for detection of local myocardial perfusion defects, but sensitivity and specificity need further clinical validation. Additionally, both CMR and SPECT possess relatively low sensitivity (67% CMR and 59% SPECT, respectively) and specificity (61% CMR and 72% SPECT, respectively) values for the diagnosis of traditional coronary artery disease (CAD), suggesting that myocardial perfusion imaging alone is capable of producing false positive and false negative diagnoses (*19*). The limited spatial resolution of traditional 64-slice computed tomography (CT) (625 μm/pixel) and invasive angiography (250 μm/pixel) *(20)* further complicates the diagnosis of coronary MVD due to the fact that approximately 90% of affected arterioles are smaller than 120 μm in diameter *(21)*, a resolution that surpasses the technical ability of modern day clinical imaging modalities. So novel sensitive molecular imaging approaches are essential for early diagnosis of coronary MVD.

Previous work in a rat (*22*) and mouse (*23*) model of high fat diet has demonstrated the ability to create pre-clinical models that exhibit impaired myocardial perfusion reserve without obstructive CAD; however, the location of coronary obstruction in these models was only found at the capillary levels, and not at arterioles. The photochemical reaction (PCR) approach is a technique originally pioneered by Watson et al. (*24*), who took advantage of the interaction of rose bengal and low energy visible light in mice to occlude cerebral arteries by microthrombus formation. Rose bengal can bind to the endothelium, resulting in endothelial dysfunction upon activation by green light. The mechanism behind PCR is that singlet oxygen converted from oxygen can directly peroxidize intracellular lipids and proteins, and that the resultant endothelial dysfunction specifically attracts and stimulates platelet aggregation (*25*). In the present study, we hypothesized that a high specificity and sensitivity FXIII targeted radiolabeled probe can serve as a biomarker for cross-linked thrombi in the microvasculature, and thus an indicator for underlying coronary MVD. We utilized the PCR approach to locally induce ROS, focal endothelial injury, and subsequent formation of microthrombi in coronary arterioles to establish a novel pre-clinical model for coronary MVD.

Methods and Materials

Animals

8-12-wk-old female C57BL/6J mice (Charles River, Indianapolis, ME) were used in this study. These mice were housed in groups, in a light- (12-h light cycle) and temperature- (69 °F) controlled environment. They were fed a pellet rodent diet, *ad libitum,* and had free access to water pre-procedure. For the first 3 d post-thoracic procedure, mice were housed individually and provided with a soaked diet. For the remaining days, these mice were housed as groups analogous to the pre-procedure. The study conformed to the guidelines for the Care and Use of Laboratory Animals published by the US National Institutes of Health (NIH Publication No. 85-23, revised 1985) and was approved by the Institutional Animal Care and Use Committee.

In vitro experiment to optimize PCR parameters

Primary cells isolation and culture

Primary endothelial cells (ECs) from 10 adult mouse hearts were isolated, as previously described *(26, 27)*. Cultured ECs were harvested and confirmed by their 'cobblestone' morphology and positive expression of CD31 using monoclonal antibody to the mouse CD31 antigen (Caltag Laboratories, Burlinga-

me, CA, USA).

In vitro PCR

Seeded ECs were incubated with concentrations of freshly prepared rose bengal (0, 0.002, 0.01, 0.05 mg/ml) (Sigma-Aldrich, St. Louis, MO, USA) in the dark, and subsequently illuminated by a focal green light (with emission 540 nm) with 3300 K energy (KL1500 LCD, Zeiss) for various periods of time (0, 2, or 4 min). After 4 h of incubation at 37 °C, the maximum endpoint absorbance was read at 490 nm on a THERMOmax reader (Molecular Devices, Sunnyvale, USA) for the (3-(4,5-dimethylthiazol-2-yl)-5-(3-carboxymethoxyphenyl)-2-(4-sulfophenyl)-2H-tetr azolium) (MTS) assay, in which the absorbance reflects total survival cell numbers.

To confirm that singlet oxygen was the primary oxidant generated in PCR protocols *(28),* we stained treated ECs for singlet oxygen and total ROS. Immediately after different interventions, 100,000 ECs were left *in situ* with 1 nM sodium azide (singlet oxygen scavenger, NaN3, to increase the life-time of singlet oxygen) for 1 min. The cells were then incubated with singlet oxygen sensor green (SOSG) for 4 min, washed twice with PBS, and co-stained with 1:1000 4',6-diamidino-2-phenylindole (DAPI) for 15 min.

For total ROS staining, 100,000 primary ECs were plated in each well and cultured as previously described. CellROX® Oxidative Stress Reagent (Cat No: C10444, Life Technologies, Carlsbad, CA) was added at a final concentration of 10 µM to these ECs and incubated for 2 h. Rose bengal was incubated for 30 min and light illumination was on for 0, 2, or 4 min. The cells were then left at 37 °C incubator for an additional 12 min. Cells were fixed with 4% formaldehyde for 15 min, washed twice with PBS, and then co-stained with 1:1000 DAPI for 15 min.

Finally, the stained cells were examined within 24 h after DAPI staining by a Leica 4-laser confocal microscope and representative images were taken.

In vivo experiments to validate the MVD model

To establish a mouse model of coronary MVD, the optimal parameters of PCR were translated to *in vivo* experiments. 64 mice, weighing 19 to 22 g, were randomly assigned to rose bengal only (n = 8), light only (n = 8), a combination of rose bengal and light (PCR, n = 36), or sham surgery (n = 12). Mice were anesthetized using inhalation of 1.5-2% isoflurane in a closed chamber. The cervical skin was cut in the midline. Tracheal intubation was performed via an oral route under microscopic guidance, and subsequently connected to a rodent ventilator with a stroke volume of 0.2–0.25 ml and a respiration rate of 120 strikes/min. The plane of anesthesia for surgery was regulated by delivery of 2% isoflurane through a vaporizer with 100% oxygen. All surgical manipulations were performed under a dissecting microscope, maintaining aseptic conditions on a heated surgical pad at 37 °C.

PCR-induced coronary MVD model

Using the neck incision, the left jugular vein was exposed and catheterized with a PE10 tube. A small left anterior thoracotomy was performed at the 4th intercostal space after mechanical ventilation. To mimic the small size of MVD lesions in the clinical environment (21), a home-made extension with a 2-mm aperture, connecting to a fiber-optic bundle of the cold light source was placed on the surface of the anterolateral heart. 0.1 ml rose bengal at 10 mg/ml was delivered via the PE10 catheter. One min later green light was turned on for 4 min to activate the localized rose bengal. The chest cavity was closed with a 6-0 prolene suture and mice were gradually weaned off the respirator. Thirty min later, fully conscious animals were returned to their original cages. Buprenorphine was administered subcutaneously at 0.05 mg/kg, once pre-emptively, then every 12 h for 72 h. The survival rate for the thoracic surgery was ~92% (173/188). Some mice failed to recover from anesthesia or had excessive bleeding during the procedure and thus were excluded from further experimentation.

Transmission electron microscopy (TEM) to assess endothelial integrity

A total of 6 mice were evaluated with TEM. 4 mice were sacrificed either 3 h (n = 2) or 24 h (n = 2) after PCR was applied on the heart surface, and 2 mice served as controls with sham surgeries. Hearts from these mice were perfused with 2.5% glutaraldehyde in phosphate buffer. Heart tissues were micro-dissected to 1 to 2 mm and fixed in 2.5% gluteraldehyde and 2% paraformaldehyde in 0.1 M sodium cacodylate buffer pH 7.4 for 1 h. Samples were further post-fixed with 1% osmium tetroxide (OsO_4) for 1 h, en-bloc stained in 2% uranyl acetate in maleate buffer pH 5.2 for another 1 h, then rinsed, dehydrated in an ethanol series, infiltrated with Epon 812 resin and baked over-night at 60 °C. Hardened blocks were cut using a Leica UltraCut UCT microtome. 60 nm sections were collected and stained using 2% uranyl acetate and lead citrate. Samples were all viewed by FEI Tencai Biotwin Transmission Microscope at 80 Kv. Images were taken using Morada CCD and iTEM (Olympus) software.

Fluorescent coronary angiography to examine coronary microvascular perfusion patterns

3 h and 24 h after application of PCR, 0.2 ml fluorescein isothiocyanate (FITC)-dextran (12.5 mg/ml, Sigma) was administered intravenously and circulated for 1 min before sacrifice in 4 mice (n = 2 per time point). The hearts were harvested and vibratome cross sections (8 serial 60 µm sections/heart) were observed with a Leica 4-laser confocal microscope. The left ventricle (LV) septal walls served as internal-controls for the anterior-lateral PCR regions.

Echocardiography to assess cardiac function

To determine whether PCR-induced MVD led to cardiac dysfunction, mice (n = 12) underwent serial echocardiography (baseline, 24 h, 3, 7, and 14 d) utilizing a commercially available system (the Vevo 2100, Fujifilm, VisualSonics Inc) before and after induction of coronary MVD. The mouse was positioned on an imaging stage with a heating system to maintain physiological body temperatures during imaging. Electrocardiographic leads were attached to each limb. B-mode and M-mode two-dimensional (2D) images were obtained in a parasternal short- and long-axis views. Images from these studies were recorded digitally for subsequent analysis. Measurements from the recorded tracings were averaged over at least five cardiac cycles for systolic function. In the M-mode long-axis images, LV end diastolic and systolic dimensions (EDD, ESD) were measured at the mid-papillary muscle level. LV percent fractional shortening (%FS) and ejection fraction (EF) were calculated using B-mode short-axis images. For assessing diastolic parameters, mitral inflow velocities were determined by pulsed Doppler imaging. The peak early (E) and late (A) diastolic velocity were measured from the mitral inflow velocity pattern. The mitral annular motion velocity was recorded at the septal site in the apical 4-chamber view using pulsed tissue Doppler. Peak early diastolic velocity (e′) was measured, and the ratio of peak early diastolic transmitral flow velocity to annular velocity (E/e′) was calculated. Because E/e′ has been accepted as a surrogate marker of LV filling pressure, particularly in heart failure with preserved ejection fraction in the clinical setting, (*29*) we used E/e′ as an index of diastolic function in our mice.

Specimen micro-CT coronary angiography to assess the macrovascular and microvascular tree

Thirty-two mice with rose bengal only, light only, PCR, or sham surgery (n = 8) were sacrificed 24 h after interventions with the heart being arrested at the end of diastolic phase using saturated potassium chloride. To confirm the presence of PCR-induced injury in the coronary micro- or macro-vasculature, the coronary vessels of mice were retrogradely perfused with 20% bismuth in 5% gelatin for casting of the coronary vasculature at 100-110 mmHg driving pressure, as previously described *(30-33)*. The scan parameters for the microCT scanner were as follows, 2960 ms exposure time, 60 kV, 100 µA current, 360°, and 720 views. The raw micro CT images with a vff format of each heart was initially reconstructed with Microview software with calibrated attenuation values for air, water, and bone. The reconstructed images were saved in dicom format and transferred to an advanced workstation. The intervention-targeted region of the myocardium (2-mm diameter) with surrounding area (total 4 mm diameter transmural cylinder) was segmented based upon anatomic landmarks and further re-batched into cross-sections with 16 µm interval space after thresholding these images. The "Analyze participles" function (Image J, Bethesda, Maryland) was used for counting the relative arterial amount in cross-section microCT images after binary images were made in 8 bits and vessels were assigned to different groups per cross sectional diameter of each vessel.

Histological analysis to assess inflammation and myocardial infarction

10 mice were sacrificed at five different time points post-MVD induction (n = 2 per time point at 3 h, 24 h, 3 d, 7 d, and 14 d). An additional 2 mice with sham surgery were also histologically assessed (3 h-post procedure). After paraffin embedding, 6-µm-thick sections were cut from each sample. Sections were stained with hematoxylin and eosin or Masson trichrome, and subsequently examined at × 200 magnifications for evaluating the tissue response.

Immunohistochemistry staining for oxidative biomarkers (4-Hydroxy-2-Nonenal and Nitrotyrosine) and inflammatory markers (CD45 & CD68)

For immunohistochemistry analyses, 10 mice were sacrificed at five different time points post-MVD induction (n=2 per time point at 3 h, 24 h, 3 d, 7 d, and 14 d), and an additional 2 mice with sham surgery were also assessed to match previously described histological analyses. Frozen sections (6 µm thick) were cut with a cryostat, mounted on glass slides, and fixed for 10 min with acetone at -20 °C. Sections were pre-incubated with 10% normal goat serum and / or bovine serum albumin (BSA) for 15 min to block nonspecific bindings of antibodies. These sections were incubated with either a monoclonal antibody to 4-hydroxy-2-nonenal (4-HNE; Oxis; diluted 1:10) or a

polyclonal antibody to nitrotyrosine (Sigma; 1:500); or mouse anti-mouse monoclonal CD68 antibody (ab955) (1:200 dilution; clone KP-1; ABCAM), rat anti-mouse CD45 (1:200 dilution; clone 30F-11; BD Biosciences — Pharmingen), or nonimmune rat IgG (1:100 dilution; DakoCytomation A/S) overnight at 4 °C and the secondary antibody (fluorescent anti-mouse or anti-rabbit IgG reagent 1:500 dilution; Invitrogen) for 1 h at room temperature. The negative control was processed in a similar fashion by replacing the first antibodies with nonimmune (rat) IgG. The fluorescent reaction product was visualized utilizing 4-laser confocal microscope.

Quantitative real-time polymerase chain reaction

To understand the composition of microthrombi, mRNAs of α-fibrinogen, tissue plasminogen activator (tPA), plasminogen activator inhibitor-1 (PAI-1), α2-antiplasm, FXIII a unit (FXIIIa), and FXIII b subunit (FXIIIb) were amplified and quantified using real-time quantitative polymerase chain reaction in 20 mice at five different time points post-MVD induction (n = 4 per time point).Total RNA was extracted from the region of MVD and septal myocardium using TRIzol (Lifetech, Tokyo, Japan) per the manufacturer's protocol and converted to cDNA using iScript cDNA Synthesis Kit (Bio-Rad Laboratories, Inc.) with random hexamer primers. Reactions were performed using the following protocol: 50 °C for 2 min, 95 °C for 10 min, and 40 cycles at 95 °C for 15 secs and 60 °C for 1 min. Target mRNA amounts were normalized to 18S ribosomal RNA. Results were expressed as the percent of ribosomal RNA-normalized target mRNA in MVD regions and control septal regions. The results were analyzed using the iQ5 Optical System (Bio-Rad).

Early detection of coronary MVD with a molecular probe targeting FXIII activity in mice

Reagents and substances

NC100668 and AH110563 (inactive analogue) were provided by GE Healthcare (Little Chalfont, UK) in a lyophilized kit and prepared by following the company's instructions. The chemical synthesis of NC100668 has been described previously *(34)*. Briefly, a fragment of α_2-antiplasmin, Acetyl-Asn-Gln-Glu-Gln-Val-Ser-Pro-3-iodo-Tyr-Thr-Leu-Leu-Lys-Gly-NC 100194, was synthesized by solid-phase peptide synthesis. This 13-amino acid substrate can be recognized by the active FXIII (FXIIIa) and covalently binds to fibrin by means of the transglutamase activity of FXIIIa (*35*). NC100194 (N,N-bis(N-(1,1-dimethyl-2-(hydroxylimino-)propyl)aminoethyl)aminoethylamine) is a ^{99m}Tc-chelator. To evaluate the molecular specificity of NC100668 for the activity of FXIIIa, a scramble control imaging agent (AH110563) was engineered similarly, which has limited affinity for FXIIIa (*34*). Each kit contained approximately 90 µg of ligand plus buffer, Sn^{2+} as reductant, radio-stabilizer as well as methylene diphosphonic acid, which was added to each kit as an Sn^{2+} solubilize. These excipients facilitated the radiolabeling of the test substance following reconstitution with up to 5 ml sodium (^{99m}Tc) solution, containing approximately 2.5 GBq ^{99m}Tc. Reconstituted kits were heated at 60–65°C for 10–12 min in a water bath and then cooled to room temperature before injection.

Table A. Primers sequences used by real-time quantitative polymerase chain reaction.

	sense primer sequence	antisense-primer sequence
α-fibrinogen	5'-GTCTGATG GCACTGGAGACTGG-3'	5'-TTCGCTTCCTGCCTCGTCT GCC-3'
prothrombin	5'-CAAGC ATTCCCGAACCAGATATG-3'	5'-TCCTCGCTTGGTGTCATTC ACC-3'
tPA	5'-CTGAGGTCACAGTCCAAG CAATGT-3'	5'-GCTCACGAAGATGATGGT GTAAAGA-3'
PAI-1	5'-GACAGCACTGTCAGGGTC CATAG-3'	5'-GCGGTCCTCCTTCACAAA GCTC-3'
α2 anti-plasmin	5'-AATTGTTCCAGGGCCCAG ACCTTCGT-3'	5'-GTCCTCCATGATGAAGAA GAGGAAGGG-3'
FXIIIa	5'-ACAATGATGCCAATCTGC AA-3'	5'-CACCGAATCCTTGGTGAG TT-3'
FXIIIb	5'-CGACGCAGAGAACATTC AAA-3'	5'-CCCAGTCTGCTTCCCTGT AG-3'

Bio-distribution of ^{99m}Tc-NC100668 in mice with or without coronary MVD at 24 h post-intervention

To determine whether active FXIII is a specific biomarker for MVD, 24 young mice (19-22 g) were randomly assigned to three different groups (green light only, rose bengal only, or combination) for bio-distribution of ^{99m}Tc-NC10668. 24 h after intervention, a bolus of 1 mCi ^{99m}Tc-labeled NC100668 was injected into the left jugular vein and permitted to circulate for 1 h. Mice were then sacrificed and different organs: heart (anterolateral region of the left ventricle, the posterior wall and the septal regions of the left ventricle as a normal myocardium control), blood, lung, chest wound, soleus muscle, liver, spleen, kidney, and pancreas, were collected into pre-weighed plastic tubes. Radioactivity was measured using a gamma well counter (Cobra 2000, Packard Instruments, Meriden, Connecticut) and corrected for background activity, decay time, tissue weight, and spill-up and spill-down correction *(36)*.

The time course of ^{99m}Tc-NC100668 and ^{99m}Tc-AH110563 in mice with coronary MVD

To determine the time course of FXIII activity and the effect of hyperpermeability on radiotracer uptake, 80 young mice (19-22 g) were randomly

assigned to MVD induction at five different time-points (3 h, 24 h, 3 d, 7 d, and 14 d, n = 8 per time point per trace). On the terminal day, a bolus of 1 mCi ^{99m}Tc-labeled NC100668 or ^{99m}Tc-AH110563 was injected into the left jugular vein and permitted to circulate for 1 h. Blood, the area of induced MVD, and the uninjured normal myocardium were collected for assessment of radiotracer uptake via GWC, as previously described *(37)*.

In vivo SPECT-CT imaging of FXIII activity in murine coronary MVD

To explore the feasibility of *in vivo* molecular imaging of MVD, 14 mice with coronary MVD were injected intravenously with ~1 mCi of ^{99m}Tc-NC100668 and serially scanned using a list mode acquisition at different time points (3 h, 3 d, 7 d, and 14 d after MVD induction). Imaging was performed with a hybrid dual-headed microSPECT-CT small animal scanner (X-SPECT, Gamma Medica-Ideas, Northridge, CA) equipped with 1-mm pinhole collimators. Mice were placed on the animal bed in the supine position with legs secured in an extended position. 1 h after radiotracer injection, mice underwent high resolution anatomical CT imaging (512 projections, 50 kV/600 µA energy) after 250 µl omnipaque (350 mg I/ml) was injected intravenously. Mice underwent continuous SPECT imaging (32 projections, 60 sec/projection per head) with a 20% energy window centered at 140 keV. The microSPECT and microCT images were reconstructed and fused to facilitate localization of radiotracer uptake and quantification. The relative uptake of ^{99m}Tc-NC100668 was analyzed using volumes of interest generated from the SPECT images with methods developed and validated in our laboratory *(38)*.

In an additional subset of 6 mice, hybrid micro-SPECT/CT imaging was also performed at 3 h post- MVD induction, 15 min following the injection of ^{201}Tl (for perfusion assessment), and 60 min after ^{99m}Tc-NC100668 injection. ^{99m}Tc-NC100668 (1 ± 0.05 mCi) was first administered into the jugular vein. Forty-five min later, ^{201}Tl (72 ± 3 µCi) was injected using the same route. Simultaneous dual-isotope SPECT imaging was then performed 15 min after ^{201}Tl injection to acquire data in both ^{201}Tl and ^{99m}Tc energy windows. Projections were acquired for 45 seconds per view in 64 views over 180 ° [radius of rotation (ROR) 3.0 cm, field of view (FOV) 3.83 cm]. The projection data was acquired in a 128 x 128 image with a pixel size of 0.345 cm. The energy windows were 20% wide and centered at 140.5 keV for ^{99m}Tc; windows of 30% width centered at 72 keV and 15% centered at 167 keV were used for ^{201}Tl. After each SPECT scan, low dose CT images were acquired and used to generate attenuation maps for both the ^{99m}Tc window and ^{201}Tl windows.

Statistical Analysis

All results are expressed as means ± standard deviation (SD), with a testing level (α) of 0.05 and p values as indicated. $p \leq 0.05$ signifies statistical significance. The radioactivity in selected organs was calculated as the percent injected dose per gram of tissue (%ID/g). One and/or two-way Analysis of Variance (ANOVA) test were used to determine whether there were any statistically significant differences between the means of three or more independent groups. If the one-way ANOVA returned a statistically significant result, a post-hoc Tukey test or student *t* test was used as a followed-up to determine which specific groups differed from each other using IBM SPSS statistics (V22).

Results

PCR parameters were optimized

When primary ECs were exposed to different combinations of rose bengal concentrations and illumination times of green light, ECs underwent progressive levels of oxidative stress, injury, and apoptosis. Evaluation of cell viability, singlet oxygen, and total ROS are shown in Fig. 1. At the highest concentration of rose bengal (0.05 mg/ml), with or without light illumination, less than 15% of ECs survived, with the highest fluorescent signals of singlet oxygen and ROS suggesting that, at this concentration, rose bengal alone had saturated toxicity. Light only, regardless of the illumination time, had no cytotoxic effects on primary ECs. Cells treated with a combination of rose bengal at a concentration of 0.002 or 0.01 mg/ml and green light exhibited time-dependent toxicity with mild fluorescent singlet oxygen and ROS production. These results demonstrated that PCR can induce cellular injury from oxidative stress (singlet oxygen or ROS), which can be precisely regulated by dosage (Fig. 1). Immunohistochemistry staining results demonstrated endocytosis of rose bengal only at the highest concentration (0.05 mg/ml rose bengal), with significant fluorescent intensities of singlet oxygen or total ROS (Fig. 1B). These important *in vitro* studies established the optimal concentrations of rose bengal (0.002-0.01 mg/ml) and light illumination (4 min) required for oxidative stress production in primary ECs. The auto fluorescence of rose bengal allowed us to determine a plasma half-life of approximately 5 min. With such a short half-life and the need for systemic delivery in mice, 0.1 ml rose bengal at 10 mg/ml combined with 4 min illumination was ultimately utilized for *in vivo* experimentation.

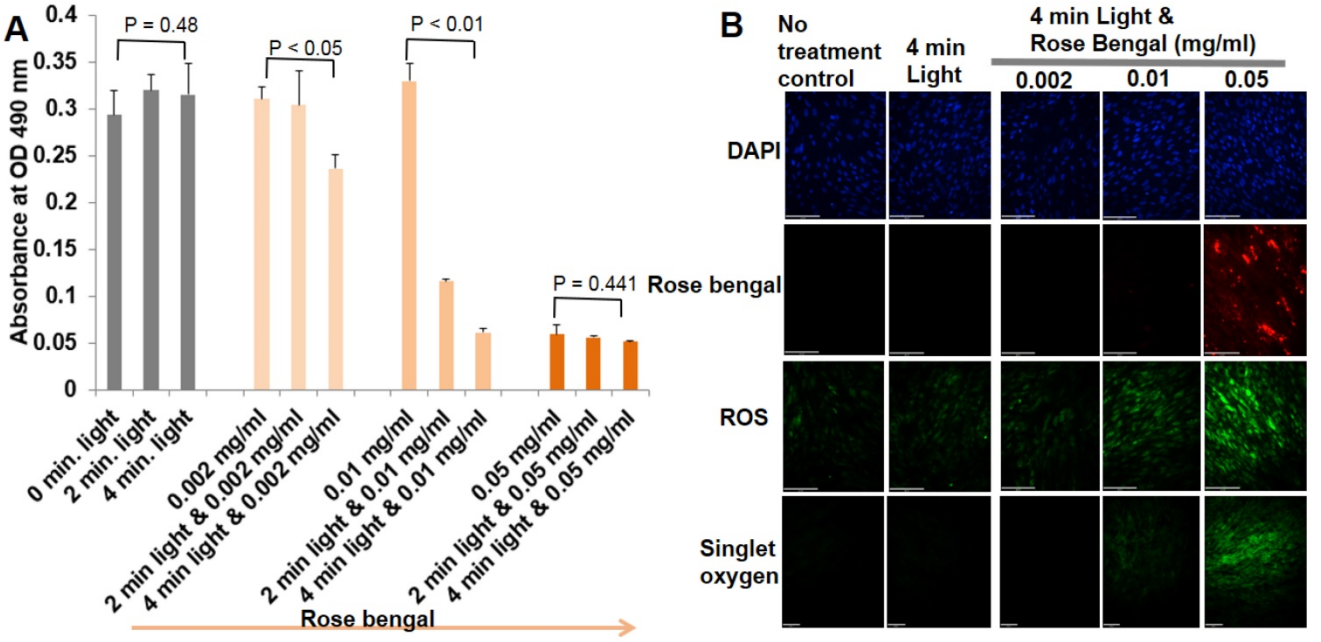

Figure 1. Optimal PCR parameters were determined based on their effects on primary EC viability and oxidative stress. (**A**) Cell viability was determined by the MTS reduction assay as described in Materials and Methods. The amount of 490nm absorbance in the presence of different concentrations of rose bengal and various periods of illumination. Each panel is a composite of three experiments. There were statistically significant differences in EC viability between group means (rose bengal concentration, period of green light illumination, and their interaction), assessed by two-way ANOVA ($p < 0.01$). One-way ANOVA was further used for the effect of different light illumination periods on the same concentration of rose bengal in Fig 1A. One Way ANOVA p-values were reported. The post-hoc Tukey test was finally used to indicate which combinations of rose bengal and green light illumination were significantly different from another groups. (**B**) Representative immunohistochemical staining of primary ECs for detection of singlet oxygen and ROS (n=4).

Focal endothelial injury was induced only in coronary microvasculature in the coronary MVD model

In vivo models were then developed based on the optimization and techniques as described in Methods and Materials. Structural evaluation with TEM demonstrated that PCR reduced the arteriole ECs sizes with loss of vesiculo-vacuolar organelles, broke the cell-cell tight junction, and resulted in extraluminal leakage of circulating components at 3 and 24 h post-PCR (Fig. 2). These changes reflect what has been previously observed in the early stages of clinical MVD: endothelial injury in the microvasculature *(39)*. Cardiomyocytes demonstrated injured mitochondria 3 and 24 h post-PCR when compared to the normal myocardium of control sham operated mice (Fig. 2).

"No flow zone" and arteriole rarefaction with normal epicardial coronaries were discovered in the coronary MVD model

We next investigated myocardial perfusion abnormalities and coronary branching in a PCR-treated region. Fluorescent myocardial perfusion studies demonstrated anterolateral perfusion defects by confocal microscopy (Fig. 3). Well-perfused fluorescence in septal areas indicated normal flow (both micro- and macro-vessels) (Fig. 3A & 3C). Absent fluorescence (no-flow zone) with residual rose bengal fluorescence in the epicardial coronaries (anterolateral walls) indicated that the PCR had successfully targeted the microvasculature (Fig. 3B & 3D). Based on reduced fluorescence at 24 h, microthrombi appeared to progress over time, indicating microvascular obstruction with subsequent non-transmural myocardial infarction. Both microCT and macroscopic imaging (Fig. 4) showed a single non-transmural MVD lesion (2 ~ mm). In exploring the resultant anatomical level of coronary vascular occlusion, high-resolution microCT coronary angiography demonstrated focal small arteriole rarefaction (<128 um, $p < 0.05$) with large coronary arteries of normal size ($p > 0.05$) (Fig. 4) in PCR-treated mice when compared to the control groups (sham operated, light only, rose bengal only).

Cardiac function was preserved in the coronary MVD model

To further investigate whether PCR-induced injury resulted in cardiac dysfunction, mice (n=12) were serially assessed by echocardiography before and after induction of MVD. Left ventricular mass slightly increased at 24 h (54.97 ± 9.67 mg, $p > 0.05$), 1 wk (55.13 ± 9.17 mg, $p > 0.05$), and 2 wk (61.22 ± 8.46 mg, $p > 0.05$) after induction of MVD when compared to baseline (52.56 ± 5.67 mg). The end systolic diameter (ESD) averaged 2.69 ± 0.19 mm while the end diastolic diameter (EDD) averaged 3.61 ± 0.28 mm

in the basal state. MVD-induced mice did not exhibit obvious changes in myocardial wall thickness, as both the average LV-ESD and LV-EDD were slightly decreased in the PCR-treated groups at the time of the follow-up assessment (Fig 5A, $p > 0.05$). FS, EF, and E/e' did not significantly change before and after MVD induction ($p > 0.05$ versus baseline) (Fig. 5B & C). Such findings are consistent with human coronary MVD, where cardiac function may be preserved.

Oxidative stress and infiltration of inflammatory cells were present in the coronary MVD model

In investigating oxidative stress, PCR treatment significantly increased 4-HNE staining within MVD-regions, being more pronounced over time (Fig. 6A). Additionally, nitrotyrosine, a marker of peroxynitrite, was also enhanced in MVD regions, reaching a peak on d 14 when compared to control myocardium (Fig. 6A). In mice with coronary MVD, infiltration of inflammatory cells in the ischemic and infarcted myocardium began on d 3, increased over time until d 7, and then decreased on d 14 (Fig. 6B). These results indicate that in addition to the initial PCR-initiated ROS infiltration, inflammation also contributed to secondary ROS in our MVD model.

Gene expression demonstrated a pro-thrombotic and impaired fibrinolytic status in the coronary MVD model

Alpha-fibrinogen, FXIII a subunit, and FXIII b subunit expression significantly increased at 3 h post-MVD induction when compared to normal myocardium (septal wall), indicating a pro-thrombotic status in the early stages of this ROS induced MVD (Fig. 7A-C). Additionally, gene expression ratios for tissue plasminogen activator (tPA), plasminogen activator inhibitor-1 (PAI-1), and α2-antiplasm were significantly increased at 3 and 24 h post-MVD induction when compared to normal myocardium, confirming the presence of impaired anti-fibrinolytic status (Fig. 7).

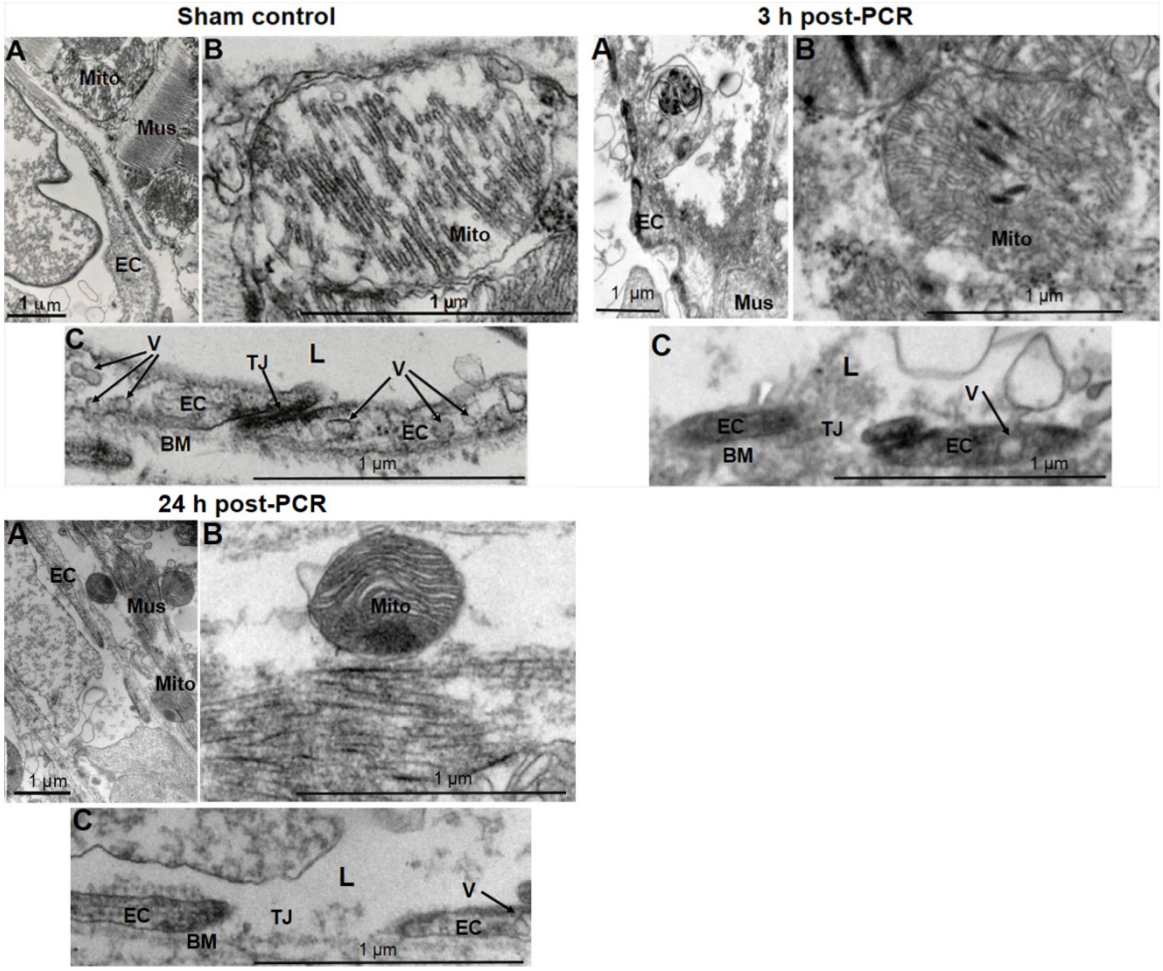

Figure 2. Focal endothelium injury was induced by PCR applied to the microvasculature. Representative transmission electron microscopic images (1-2 images/mouse, n = 2 mice/group) documented PCR-induced endothelial injury. 3 h and 24 h post-PCR samples exhibited endothelial injury (A & C) characterized by loss of endothelial integrity, reduced size of ECs, loss of the vesiculo-vacuolar organelle (V), broken tight junctions (TJ), damaged mitochondria (Mito) (B), and disruption of the muscle contractile proteins (Mus) (A) when compared to sham control samples. L: arteriole lumen; BM: basement membrane. Scale bar 1 um.

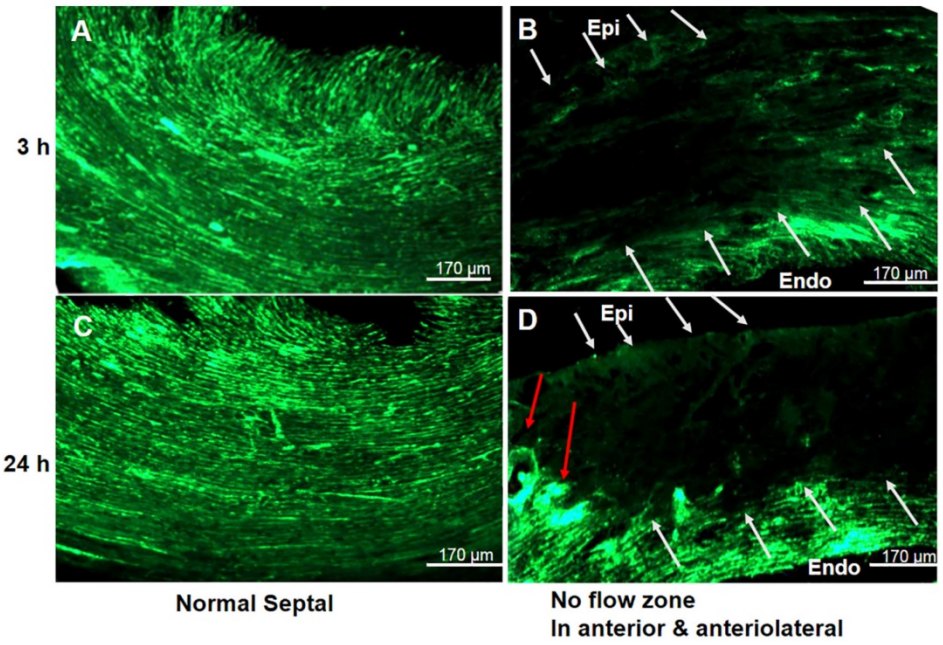

Figure 3. No flow phenomena indicated focal ischemia in the coronary PCR-induced MVD model. Representative confocal microscopy (n = 4) demonstrated the presence of a "no flow phenomena" following *in vivo* fluorescein isothiocyanate (FITC)-dextran injection, suggesting coronary arteriole luminal obstruction. (**A & C**) Fluorescent images of the contra-lateral LV septal wall at (**A**) 3 and (**C**) 24 h after PCR-induced microvascular disease (MVD) demonstrated normal perfusion. (**B & D**) Images were from an ischemia region within the illuminated photothrombotic area. Absent fluorescence of microvessels (white arrows) with intact macrovessels (red arrow) indicated PCR did target the microvasculature. Scale bar is 170 μm. Epi: epicardium; Endo: endocardium.

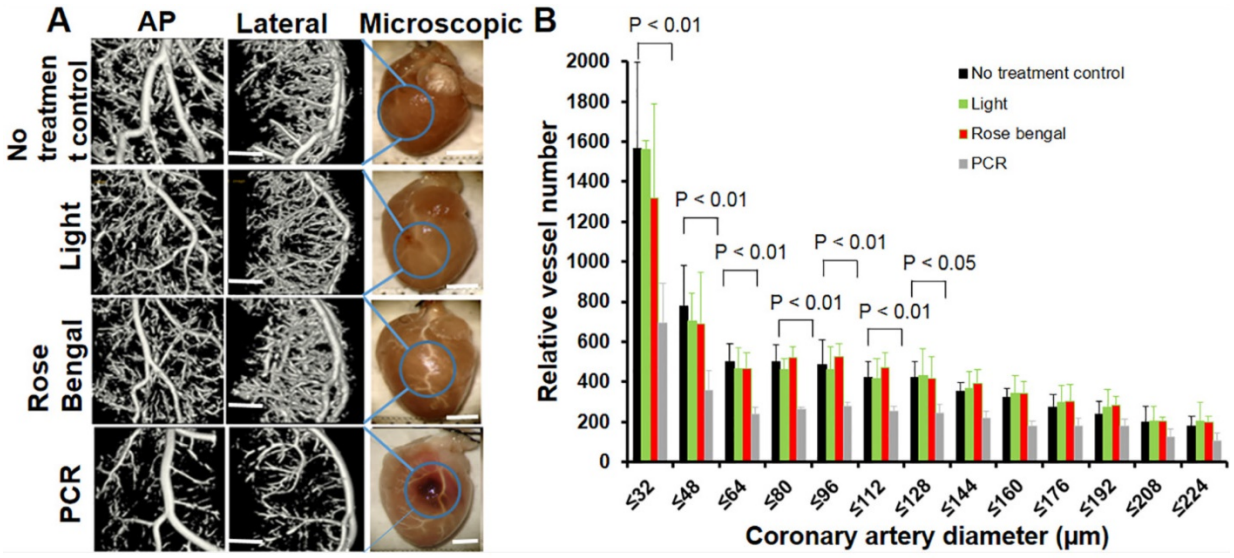

Figure 4. Coronary microvasculature obstruction with normal epicardial coronaries was induced in the coronary MVD model. (**A**) Representative coronary angiography (n = 8) from targeted regions demonstrated PCR-induced small arteriole rarefactions without changes in macrovasculature. At the same time, light only or rose bengal only had minimal effects on the macro- and micro-vascular system. Scale bar is 1 mm in Fig 4a for microCT images. Scale bar is 2 mm in Fig 4a for microscopic view. (**B**) Quantitative analysis further confirmed microvascular rarefaction (<128 um) 24 h post-PCR induction. A two-way ANOVA analysis was used to show there were statistically significant differences (defined as p-value <0.05) in relative vessel number among different interventions (no treatment control, Light, rose bengal, PCR) and among different diameters (size distributions). One-way ANOVA p-values were further used to determine difference within group (different diameter). These p-values ($p < 0.01$) were reported in Fig 4B. Pairwise comparisons were based on Tukey's test. AP: anteroposterior view of the heart; Lateral: lateral view of the heart; Microscopic: microscopic view.

Ex vivo gamma well counting detected FXIII activity in the coronary MVD model

A significantly higher percentage of injected ^{99m}Tc-NC100668 was quantified at 24 h after coronary MVD induction when compared to the same region in mice without MVD (Fig. 8A). Additionally, there was significantly higher uptake of radiotracer in the region of the chest wound (1.02 %ID/g) in MVD-induced mice due to diffusion of illumination, when compared to light-only and rose bengal-only groups. No

significant group differences were noted for radiotracer uptake in the blood, lungs, normal myocardium, pancreas, skeletal muscle tissue, kidney, spleen, or liver (Fig. 8A & 8B).

The bio-distribution of both ^{99m}Tc-NC 100668 and ^{99m}Tc-AH110563 was also evaluated in mice at five time-points following induction of coronary MVD. Peak radiotracer uptake of both ^{99m}Tc-NC100668 and ^{99m}Tc-AH110563 occurred at 3 h after PCR-induced MVD and gradually decreased over time, consistent with the covalent binding of NC100 668 to MVD (Table 1). When compared to the uptake of AH110563, ^{99m}Tc-NC100668 uptake increased by approximately 10.5-fold at 3 h, 8-fold at 24 h, and 12-fold at d 3. Meanwhile, uptake of ^{99m}Tc-AH110563 was increased by approximately 4-fold at 3 h, 3-fold at 24 h, and more than 2-fold at d 3 when compared to the septal region (internal control) of the same mouse, suggesting that microvascular leakage may contribute to enhanced radioactivity in the early stages of coronary MVD. Generally, less than 0.6% ID/g was observed in the blood regardless of the radiotracer and the time point post-MVD induction, suggesting that the circulating platelet sources of FXIII do not significantly contribute to focal radioactivity. Collectively NC100668 may be useful for the *in vivo* detection of FXIII activity in both the acute and sub-acute setting of coronary MVD.

In vivo serial microSPECT/CT Imaging detected FXIII activity in MVD

A total of 14 mice were serially evaluated using *in vivo* SPECT imaging. Fig. 8C showed representative microSPECT-CT images in a mouse at multiple time points after induction of coronary MVD (3 h, 3 d, 7 d, and 14 d). Differences in the SPECT image-derived ratios of radiotracer retention (MVD/normal septal wall) were shown in Fig. 8D. *In vivo* SPECT/CT images demonstrated a significant increase in ^{99m}Tc-NC100668 relative retention in early stages post-MVD induction [9.81 ± 0.77 fold increase at 3 h and 3.85 ± 0.33 fold increase at 3 d after the onset of MVD], whereas mice 7 d post-MVD induction only demonstrated a peak MVD lesion-to-background of 1.50 ± 0.62 (compared to 0.8 ± 0.36 in mice with 14 d MVD, $P < 0.01$), which is consistent with an expected temporal decline in FXIII activity.*(40)* MicroSPECT/CT imaging demonstrated focal enhancement of active FXIII signals in the region of MVD lesions, presumably in areas of greater thrombin. Dual isotope microSPECT/CT imaging of thallium-201 (myocardial perfusion) and ^{99m}Tc-NC100668 (FXIII activity) demonstrated myocardial perfusion defects in the anterolateral aspect of MVD-induced hearts that were localized to the site of FXIII activity focal enhancement (Fig. 8E).

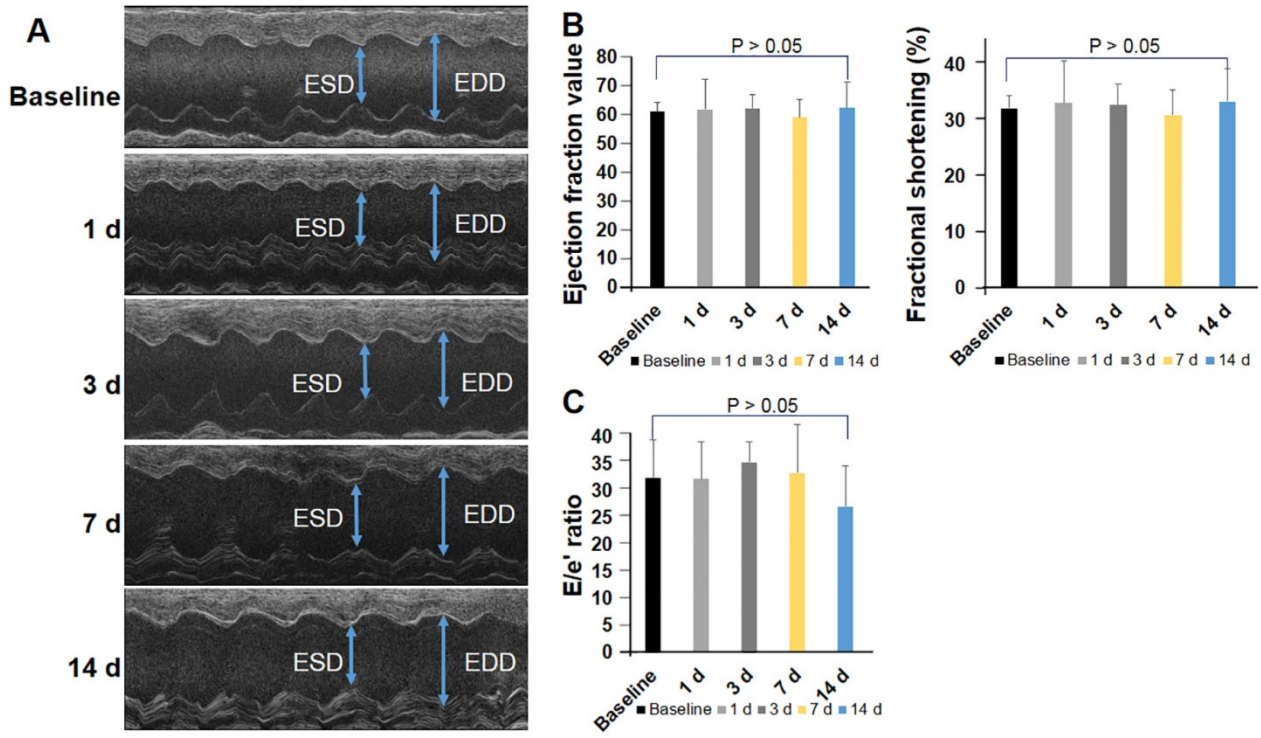

Figure 5. Global cardiac function and diastolic function were preserved in the coronary MVD model. Cardiac function was assessed by echocardiography in mice before and after MVD induction (n=12). (**A**) M-mode image of the left ventricle in the parasternal long-axis view, showing depth markers. LV-EDD: left ventricular end-diastolic diameter. LV-ESD: left ventricular end-systolic diameter. (**B**) Fractional shortening (FS) and ejection fraction were calculated from echocardiographic measurements made during the cardiac cycle. (**C**) The ratio of peak early diastolic transmitral velocity to annular velocity (E/e') was calculated and saved as an index of diastolic function. One-way ANOVA p-values are reported for the over-time effect of cardiac function in Fig 5 B & C. $p > 0.05$.

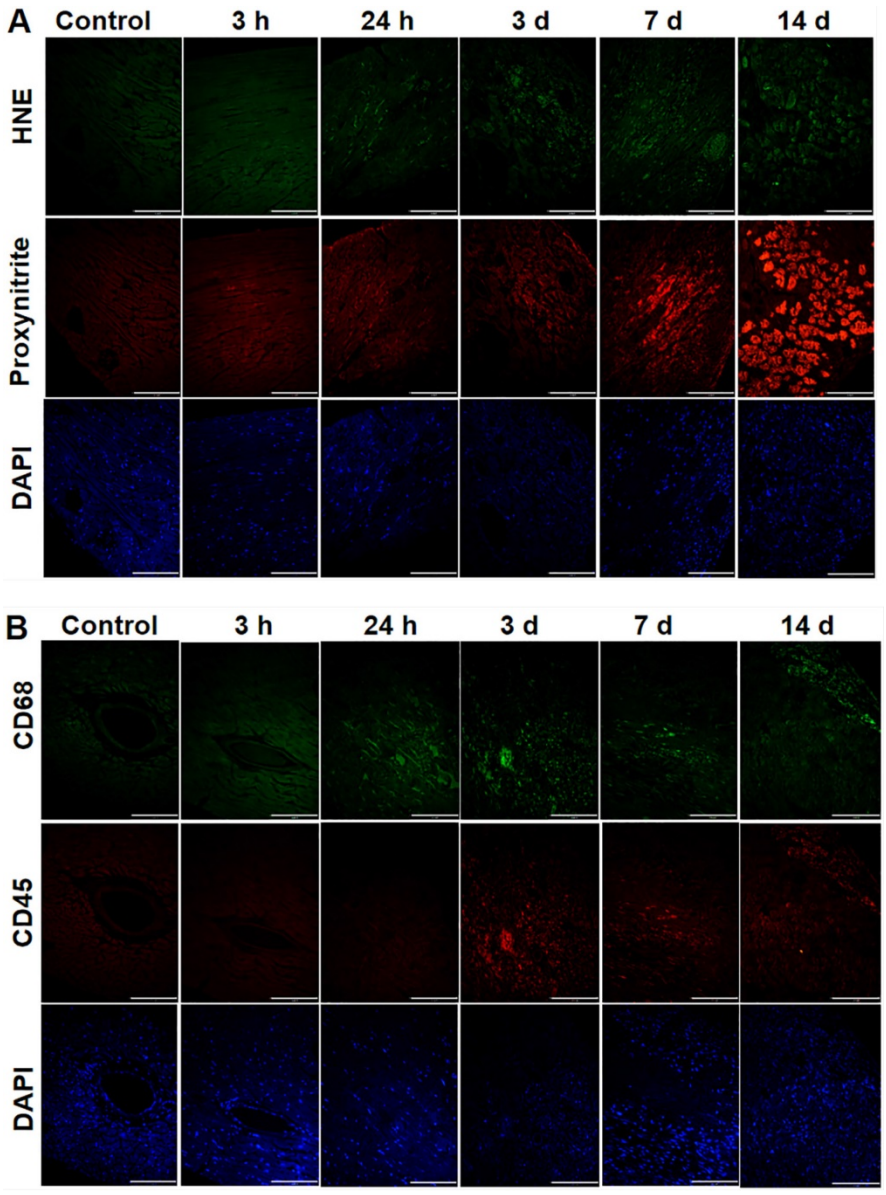

Figure 6. Oxidative stress and infiltration of inflammatory cells were present in sub-acute or chronic states of the coronary MVD model. (A) 4-4 hydroxy-2-noneal (HNE) is a marker of lipid peroxidation. Nitrotyrosine is a marker for peroxynitrite formation. The control heart without MVD was stained with anti-4-4 hydroxy-2-noneal (HNE) / anti-nitrotyrosine antibodies, which served as the negative control. Hearts with PCR-induced MVD (3 h to 3 d) was gradually stained with anti-HNE antibodies in the MVD region, and the amount of nuclei, stained by DAPI, gradually reduced. Hearts with coronary MVD (3 d to 14 d) infarcted regions were intensively stained with anti-nitrotyrosine antibodies, and the amount of nuclei, stained by DAPI, significantly increased, which might indicate inflammatory cell infiltration. **(B)** Immunohistochemical staining of CD45 and CD68 in the heart tissue from control and MVD-induced mice. CD45 is a marker of leukocytes and CD68 is a marker of phagocytes and other inflammatory cells. In hearts with coronary MVD, the PCR-illuminated region was stained positively with antibodies on 3 d, with staining intensity gradually reduced over time. At the same region, the amount of nuclei gradually decreased in the early stages, indicating myocyte damage by PCR. After 3 d, the amount of nuclei, stained by DAPI, significantly increased, which indicated accumulation of inflammatory cells. Scale bar is 120 μm. (n = 2 per time point).

Discussion

Coronary MVD is prevalent in pre-menopausal women with ischemic symptoms without obstructive CAD *(3, 4, 41)*. In these patients, positron emission tomography (PET) or CMR can detect impaired myocardial perfusion reserve (MPR) as a functional consequence of coronary MDV (*42, 43*). Myocardial ischemia can be estimated based on the duration of coronary occlusion and the delay in time to reperfusion. If microvascular occlusion can be detected earlier, such as during endothelial injury or the development of acute thrombosis, fibrinolytic strategies may be employed to avoid irreversible ischemia / necrosis as a result of occluded microvasculature. Much of the difficulty in diagnosing this early event is related to the absence of specific biomarkers for its detection. We hypothesize that FXIII, a specific biomarker for cross-linked thrombi, can be an indicator for this disease. Moreover, FXIII can be radiolabeled to predict healing after myocardial

infarction (*44*) and fluorescently labelled to detect acute thrombosis in the femoral artery (*45*). FXIII activity via molecular imaging approach had not been studied for coronary MVD detection. In the present study, we demonstrate that ^{99m}Tc-NC100668, an active FXIII-specific radiotracer, allows for non-invasive imaging and detection of MVD caused by endothelial injury and microthrombi in the coronary microvasculature. Additionally, we developed an ROS-induced mouse model for coronary MVD which recapitulates many of the features found in human MVD.

Development of a mouse model of coronary MVD simulating the same structural abnormalities observed in clinical MVD

Although the pathogenesis of clinical coronary MVD remains uncertain, a cluster of risk factors, such as obesity, hypercholesterolemia, hypertension, diabetes, and metabolic syndrome, have been proposed as contributors to coronary micro- and macro-vascular dysfunction *(3, 41, 46, 47)*. A substantial body of evidence attributes overproduction of ROS as an early event for endothelial injury *(9-11)*. In human coronary MVD, characteristic structural abnormalities of microvasculature have been identified via endomyocardial biopsies: endothelial injury *(39)*, being thickening of the arteriole wall, and narrowing or occlusion of the arteriole lumen *(48)*. For the first time, we demonstrate the creation of a pre-clinical coronary MVD model that closely mimics human MVD by producing most of these abnormalities in the mouse heart. Along with histological analysis that confirmed the presence of endothelial injury in coronary arterioles and focal ischemia/infarct in our MVD model, arteriole obstruction was confirmed by coronary microCT angiogram, with rarefaction of coronary branches in the MVD-induced region while compared to mice with sham control, light only, or rose bengal only. Quantitative analysis of microCT imaging confirmed that the size of lost arterioles was less than 128 microns in diameter, further suggesting occlusion of the microvasculature. Additionally, reflective of the characteristics of clinical MVD, neither global cardiac function nor ESD / EDD changed, consistent with the reason that clinical echocardiography is often insensitive in detecting the early stages of MVD.

Table 1. The bio-distribution of active FXIII radioactivity following injection of ^{99m}Tc-NC100668 or ^{99m}Tc -AH110563.

Organ	Tracer (%/ID/g)	3 h MVD	1 d MVD	3 d MVD	7 d MVD	14 d MVD
Blood	^{99m}Tc-NC100668	0.38 ± 0.10	0.46 ± 0.31	0.17 ± 0.07	0.17 ± 0.06	0.21 ± 0.04
	^{99m}Tc-AH110563	0.42 ± 0.14	0.39 ± 0.10	0.22 ± 0.07	0.19 ± 0.08	0.19 ± 0.03
Normal heart	^{99m}Tc-NC100668	1.04 ± 0.22*	0.51 ± 0.33*	0.44 ± 0.30*	0.13 ± 0.05	0.22 ± 0.12
	^{99m}Tc-AH110563	0.23 ± 0.11	0.18 ± 0.03	0.13 ± 0.07	0.10 ± 0.04	0.12 ± 0.03
MVD region	^{99m}Tc-NC100668	9.33 ± 1.98**	4.29 ± 1.64**	3.43 ± 1.45**	0.48 ± 0.20*	0.38 ± 0.17*
	^{99m}Tc-AH110563	0.89 ± 0.43	0.53 ± 0.10	0.28 ± 0.08	0.24 ± 0.07	0.17 ± 0.08

The data are presented as %id g^{-1} tissue in mice with different biological-age MVD (mean ± S.D. n = 8). *p < 0.05; ** p < 0.01 while compared to the scramble tracer (^{99m}Tc -AH110563).

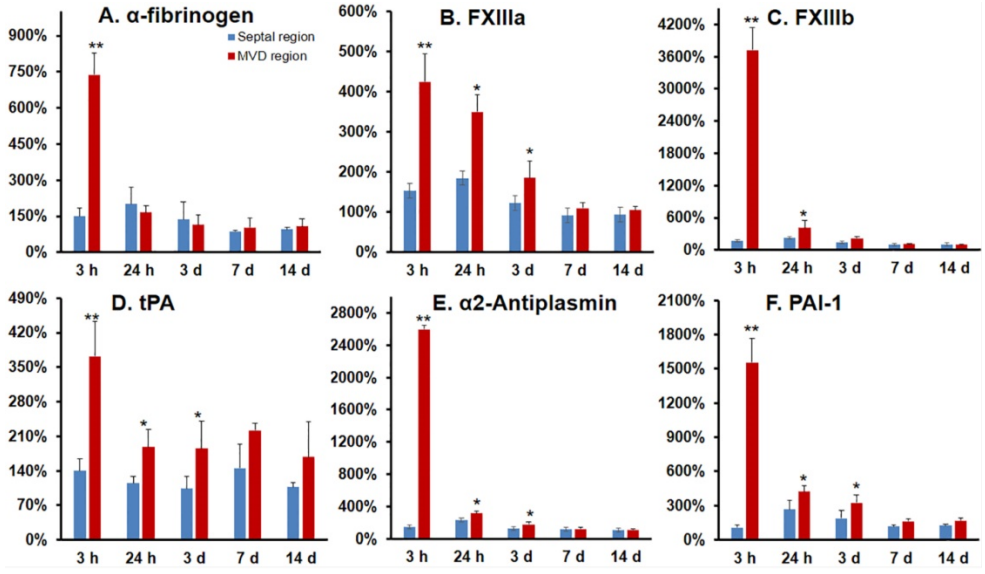

Figure 7. Gene expression demonstrated a pro-thrombotic and impaired fibrinolytic status in the coronary MVD model. Gene expression was investigated for alpha-fibrinogen (**A**), FXIII a subunit (**B**), FXIII b subunit (**C**), tissue plasminogen activator (t-PA) (**D**), α2-antiplasmin (**E**), and plasminogen activator inhibitor-1 (PAI-1) (**F**) expression in MVD regions at multiple time points after MVD induction. Both FXIII a & b subunit expression were significantly up-regulated in MVD compared with normal myocardial regions, thus confirming a role for FXIII in the early formation of MVD, as well as a pro-thrombotic and anti-fibrinolytic status in the setting of PCR-induced MVD in the first 24 h. Values are mean ± SEM, n=4. One-way analysis of variance (ANOVA) analysis was used to test whether there was a statistical significant effect of lesion aging on gene expression of key molecules. Student *t* test was used for each time point and these *p-values are reported*. ** p < 0.01; * p < 0.05

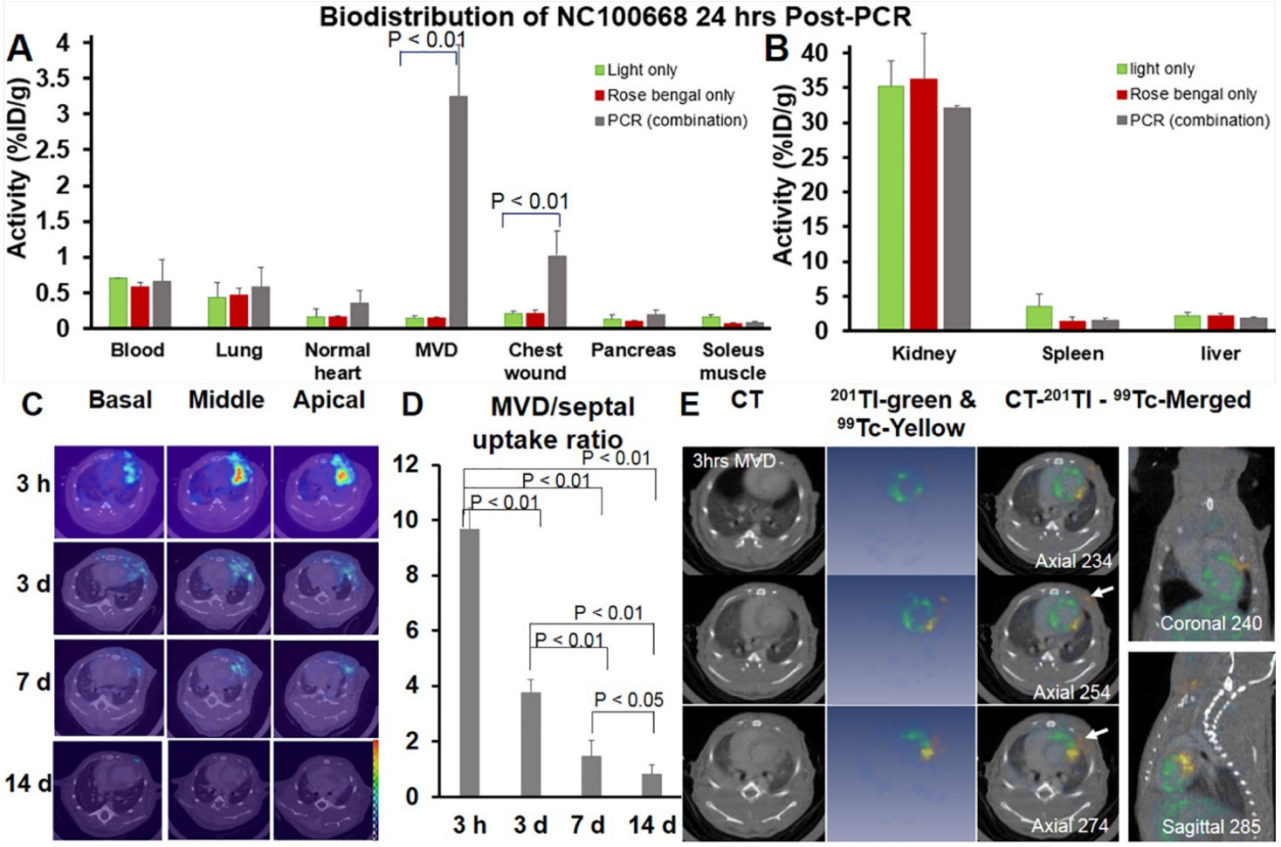

Figure 8. Both *ex vivo* gamma well counting 24 h-post MVD induction and *in vivo* serial microSPECT/CT Imaging confirmed elevated FXIII activity in in the coronary MVD model. (A) Radioactivity of FXIII in the PCR-induced MVD region increased more than 20-folds at 24 h, when compared to light only and rose bengal only groups. FXIII activity also increased approximately 2-fold in the normal region compared to the same region exposed to light only or rose bengal only. (n = 8) A one-way ANOVA analysis was used to test whether there was a statistically significant effect of intervention on NC100668 biodistribution in specific organs. These p-values ($p < 0.01$) were reported in Fig 8A. A post-hoc Tukey-test was further used, indicating that activity in the PCR group was significantly higher than those of light only and rose bengal only groups ($p < 0.01$). There were no activity differences between light only and rose bengal only groups. **(B)** Retention of ^{99m}Tc-NC100668 was dramatically increased in the kidney, liver, and spleen, indicating the clearance is comparable among the three experimental groups (PCR, light only, and rose bengal only). **(C)** Representative *in vivo* serial ^{99m}Tc-NC100668 microSPECT/CT imaging in a mouse at 3 h, 3 d, 7 d, and 14 d following induction of coronary MVD. Color-coded fused microSPECT/CT images demonstrated focal uptake of the FXIII-targeted radiotracer in the anteriolateral wall (color map scale 0-20). (n=14) **(D)** Quantitative analysis of *in vivo* SPECT/CT images showed a dramatic increase in ^{99m}Tc-NC100668 relative retention (MVD region /septal region) in the early stages after induction of MVD, which gradually decreased over time. (n = 14) A one-way ANOVA analysis was used to confirm that there was a statistically significant effect to lesion aging on NC100668 uptake (MVD/septal ratio). Pairwise comparisons were based on Tukey's test. The p-values were reported here. **(E)** Representative dual Isotopes microSPECT/CT images show focal uptake of ^{99m}Tc-NC100668, a targeted FXIII radiotracer, in the central ischemia/infarct region (color-coded yellow, white arrows), which corresponded to a ^{201}Tl myocardial perfusion defect (color-coded blue) 3 h post-MVD induction (n = 6).

Detecting coronary MVD by targeting FXIII activity within microthrombi after endothelial injury

The mechanisms for coronary MVD with no CAD have not yet been fully elucidated. Transient microthrombi secondary to the interplay among endothelium, coagulation, and inflammation might be the key link between endothelial dysfunction at the early stage and arteriole medial hyperplasia at the late stage. A long-standing hypothesis is that arterial thrombi are a classical white clot, in which activated platelets are the main cellular component, with limited fibrin. Recent evaluation of clinical intracoronary thrombus in patients with ST-elevation myocardial infarction has confirmed that coronary thrombi are primarily composed of fibrin (56%) with platelets (17%) *(49)*, which is in agreement with previous pre-clinical work that utilized a model of laser–induced thrombosis in a cremaster arteriole in mice *(26)*. In this model, fibrin was present predominantly at the head of the thrombus and at the center of the platelet plug *(50)*. In contrast, the tail portion had less fibrin, and thus small emboli can easily break off from the thrombus *(50)*. Encouraged by these seminal findings, we sought to discover if NC 100668, an active FXIII probe, would serve as a good candidate for imaging FXIII activity in the setting of cross-linked fibrin in coronary MVD. Active FXIII in the thrombi can result from plasma, as well as from platelets and inflammatory cells. Plasma FXIII can be activated by thrombin and active FXIII catalyzes covalent cross-linking of fibrin γ- and α-chains and α_2-antiplasmin and α-chains fibrin in the last step of the coagulation cascade, forming a fibrinolysis resistant clot. α_2-antiplasmin can interfere

with the binding of plasminogen to fibrin and ultimately delay the initiation of fibrinolysis.

In the present study, we demonstrated that radiotracer-based imaging may indeed facilitate non-invasive detection of coronary MVD associated with thrombus formation. Specifically, biodistribution analysis of ^{99m}Tc-NC100668 uptake revealed significant increases in FXIII activation within regions of PCR-induced MVD, which did not occur in green light-illuminated regions or rose bengal only regions. We found that FXIII activity increased by more than 20-fold over controls (light only or rose bengal only) in the PCR region 24 h after induction of MVD, in contrast to a 2-fold increase over controls in the rest of the heart (normal myocardium). Additionally, we demonstrated using *in vivo* microSPECT/CT imaging that FXIII activity within the PCR-induced MVD region peaked early, prior to the presence of fibrinolysis, and subsequently decreased over time. Some ^{99m}Tc-NC100668 uptake may have been partially attributable to hyperpermeability in the MVD region, as our EM studies revealed significant damage to endothelial cells and disruption of tight junctions, thus facilitating leakage of our targeted radiotracer outside the lumen. However, collectively, most ^{99m}Tc-NC100668 uptake was specific to cross-linked fibrin. Specifically, we demonstrated that circulating platelets had minimal contribution to the uptake of ^{99m}Tc-NC100668 by showing no difference in blood activity levels between our targeted tracer (NC100668) and our scramble tracer (AH110563) (Table 1). Additionally, by staining for CD45 positive cells in the MVD-induced region, we found a mismatch between the time course response in inflammatory cells and FXIII activity during the first 7 d following MVD induction, which suggests that monocytes were not a significant contributor to the local FXIII activity observed within the MVD region in early stages.

Limitations of the study

Some limitations to our animal model of MVD and molecular imaging of FXIII are worth noting. In humans, the major contributors to ROS are hydrogen peroxide (H_2O_2), superoxide, and hydroxyl radicals (*39, 40*). In this study, singlet oxygen was mainly induced by PCR. However, singlet oxygen can give rise to several other types of ROS, including hydrogen peroxide, superoxide, and hydroxyl radicals *(28)*. Additionally, due to technical limitations of small animal imaging, we could not reliably measure coronary flow reserve in our MVD model. This would have been useful for further validation of the presence of MVD.

Conclusions

We have developed a novel rodent model of coronary MVD with endothelial injury and thrombosis and shown that we can non-invasively assess this experimentally-induced coronary MVD *in vivo* through utilization of targeted molecular imaging of FXIII activity. Due to inherent limitations of standard clinical imaging modalities, future translation of molecular imaging of FXIII may offer novel opportunities for non-invasive detection and serial assessment of microvascular abnormalities that remain undiagnosed in the clinical setting. Additionally, the creation of our pre-clinical model of coronary MVD may assist with characterizing disease development and progression, thereby offering a model that can be utilized to explore pathological mechanisms and evaluate novel therapies.

Abbreviations

CAD: coronary artery disease; CT: computed tomography; CMR: cardiac magnetic resonance; DAPI: 4',6-diamidino-2-phenylindole; EC: endothelial cells; E/e': ration of peal early diastolic transmitral flow velocity to annular velocity; EF: ejection fraction; EDD: end diastolic diameter; ESD: end systolic diameter; FITC: fluorescein isothiocyanate; %FS: percentage fractional shortening; 4-HNE: 4-hydroxy-2-nonenal; IHC: immunohistochemistry; LV: left ventricle; MTS: (3-(4,5-dimethylthiazol-2-yl)-5-(3-carboxymethoxyphenyl)-2-(4-sulfophenyl)-2H-tetrazolium); MVD: microvascular disease; PAI-1: plasminogen activator inhibitor-1; PCR: photochemical reaction; ROS: reactive oxygen species; SOSG: singlet oxygen sensor green; SPECT: single photon emission computed tomography; TEM: transmission electron microscopy; TJ: tight junctions; t-PA: tissue plasminogen activator; UCP: unexplained chest pain.

Acknowledgments

We gratefully acknowledge GE Healthcare Co. for providing the FXIII tracer (NC100668) and scramble control tracer (AH110563). We thank Morven Graham for help with electron microscopy and Dr. Joseph A. Madri for reading the TEM photos.

Sources of Funding

This work was supported by National Institutes of Health grant 5R21HL119975 and P01HL107205 (Imaging Core) (Z.W.Z), and RO1HL122815 and RO1 HL115247 (J.H.).

Competing Interests

The authors have declared that no competing interest exists.

References

1. Storrow AB, Gibler WB. Chest pain centers: diagnosis of acute coronary syndromes. Ann Emerg Med. Ann Emerg Med. 2000; 35(5): 449-61.
2. Shaw LJ, Merz CN, Pepine CJ, Reis SE, Bittner V, Kip KE, et al. The economic burden of angina in women with suspected ischemic heart disease: results from the National Institutes of Health--National Heart, Lung, and Blood Institute--sponsored Women's Ischemia Syndrome Evaluation. Circulation. 2006; 114(9): 894-904.
3. Reis SE, Holubkov R, Conrad Smith AJ, Kelsey SF, Sharaf BL, Reichek N, et al. Coronary microvascular dysfunction is highly prevalent in women with chest pain in the absence of coronary artery disease: results from the NHLBI WISE study. Am Heart J. 2001; 141(5): 735-41.
4. Pepine CJ, Anderson RD, Sharaf BL, Reis SE, Smith KM, Handberg EM, et al. Coronary microvascular reactivity to adenosine predicts adverse outcome in women evaluated for suspected ischemia results from the National Heart, Lung and Blood Institute WISE (Women's Ischemia Syndrome Evaluation) study. J Am Coll Cardiol. 2010; 55(25): 2825-32.
5. Jespersen L, Hvelplund A, Abildstrøm SZ, Pedersen F, Galatius S, Madsen JK, et al. Stable angina pectoris with no obstructive coronary artery disease is associated with increased risks of major adverse cardiovascular events. Eur Heart J. 2012; 33(6): 734-44.
6. Lin T, Rechenmacher S, Rasool S, Varadarajan P, Pai RG. Reduced survival in patients with "coronary microvascular disease". Int J Angiol. 2012; 21(2): 89-94.
7. Mosseri M, Yarom R, Gotsman MS, Hasin Y. Histologic evidence for small-vessel coronary artery disease in patients with angina pectoris and patent large coronary arteries. Circulation. 1986; 74: 964-972.
8. Duvall WL. Endothelial dysfunction and antioxidants. Mt Sinai J Med. 2005; 72: 71-80.
9. Tousoulis D, Briasoulis A, Papageorgiou N, Tsioufis C, Tsiamis E, Toutouzas K, et al. Oxidative Stress and Endothelial Function: Therapeutic Interventions. Recent Pat Cardiovasc Drug Discov. 2011; 6(2): 103-14.
10. Valgimigli M, Merli E, Malagutti P, Soukhomovskaia O, Cicchitelli G, Macrì G, et al. Endothelial dysfunction in acute and chronic coronary syndromes: evidence for a pathogenetic role of oxidative stress. Arch Biochem Biophys. 2003; 420(2): 255-61.
11. Griendling KK, FitzGerald GA. Oxidative stress and cardiovascular injury: Part I: basic mechanisms and in vivo monitoring of ROS. Circulation. 2003; 108(16): 1912-6.
12. Halliwell B, Gutteridge JM. The importance of free radicals and catalytic metal ions in human diseases. Mol Aspects Med. 1985; 8(2): 89-193.
13. Boveris A. Mitochondrial production of superoxide radical and hydrogen peroxide. Adv Exp Med Biol. 1977; 78: 67-82.
14. St-Pierre J, Buckingham JA, Roebuck SJ, Brand MD. Topology of superoxide production from different sites in the mitochondrial electron transport chain. J Biol Chem. 2002; 277(47): 44784-90.
15. Kowaltowski AJ, Castilho RF, Vercesi AE. Mitochondrial permeability transition and oxidative stress. FEBS Lett. 2001; 495: 12-15.
16. Dahlbäck B. Blood coagulation. Lancet. 2000; 355(9215): 1627-32
17. Liu A, Wijesurendra RS, Liu JM, Forfar JC, Channon KM, Jerosch-Herold M, et al. Diagnosis of Microvascular Angina Using Cardiac Magnetic Resonance. J Am Coll Cardiol. 2018; 71(9): 969-979.
18. Feher A, Sinusas AJ. Quantitative Assessment of Coronary Microvascular Function: Dynamic Single-Photon Emission Computed Tomography, Positron Emission Tomography, Ultrasound, Computed Tomography, and Magnetic Resonance Imaging. Circ Cardiovasc Imaging. 2017; 10(8): e006427.
19. Schwitter J, Wacker CM, Wilke N, Al-Saadi N, Sauer E, Huettle K, et al. MR-IMPACT II: Magnetic Resonance Imaging for Myocardial PerfusionAssessment in Coronary artery disease Trial: perfusion-cardiac magneticresonance vs. single-photon emission computed tomography for the detection of coronary artery disease: a comparative multicentre, multivendor trial. Eur Heart J. 2013; 34(10): 775-81.
20. Leber AW, Knez A, von Ziegler F, Becker A, Nikolaou K, Paul S, et al. Quantification of obstructive and nonobstructive coronary lesions by 64-slice computed tomography: a comparative study with quantitative coronary angiography and intravascular ultrasound. J Am Coll Cardiol. 2005; 46(1): 147-54.
21. Schwartz RS, Burke A, Farb A, Kaye D, Lesser JR, Henry TD, et al. Microemboli and microvascular obstruction in acute coronary thrombosis and sudden coronary death: relation to epicardial plaque histopathology. J Am Coll Cardiol. 2009; 54(23): 2167-73.
22. Nascimento AR, Machado M, de Jesus N, Gomes F, Lessa MA, Bonomo IT, et al. Structural and functional microvascular alterations in a rat model of metabolic syndrome induced by a high-fat diet. Obesity (Silver Spring). 2013; 21(10): 2046-54.
23. Naresh NK, Butcher JT, Lye RJ, Chen X, Isakson BE, Gan LM, et al. Cardiovascular magnetic resonance detects the progression of impaired myocardial perfusion reserve and increased left-ventricular mass in mice fed a high-fat diet. J Cardiovasc Magn Reson. 2016; 18(1): 53.
24. Watson BD, Dietrich WD, Busto R, Wachtel MS, Ginsberg MD. Induction of reproducible brain infarction by photochemically initiated thrombosis. Ann Neurol. 1985; 17(5): 497-504.
25. Watson BD. chapter 4. Animal models of photochemically induced brain ischemia and stroke. In: Ginsberg MD. and Bogousslavsky J, eds, Cerebrovascular Disease-Pathophysiology, Diagnosis and Treatment, Blackwell Science, Cambridge, UK, (1998).
26. Allport JR, Lim YC, Shipley JM, Senior RM, Shapiro SD, Matsuyoshi N, et al. Neutrophils from MMP-9- or neutrophil elastase-deficient mice show no defect in transendothelial migration under flow in vitro. J Leukoc Biol. 2002; 71(5): 821-828.
27. Lanahan AA, Chittenden TW, Mulvihill E, Smith K, Schwartz S, Simons M. Synectin-dependent gene expression in endothelial cells. Physiol Genomics. 2006; 27(3): 380-90.
28. Price M, Reiners JJ, Santiago AM, Kessel D. Monitoring singlet oxygen and hydroxyl radical formation with fluorescent probes during photodynamic therapy. Photochem Photobiol. 2009; 85(5): 1177-81.
29. Kawata T, Daimon M, Miyazaki S, Ichikawa R, Maruyama M, Chiang SJ, et al. Coronary microvascular function is independently associated with left ventricular filling pressure in patients with type 2 diabetes mellitus. Cardiovasc Diabetol. 2015; 14: 98.
30. Takeda Y, Costa S, Delamarre E, Roncal C, Leite de Oliveira R, Squadrito ML, et al. Macrophage skewing by PHD2 haplodeficiency prevents ischemia by inducing arteriogenesis. Nature. 2011; 479(7371): 122-6.
31. Hofmann JJ, Briot A, Enciso J, Zovein AC, Ren S, Zhang ZW, et al. Endothelial deletion of murine Jag1 leads to valve calcification and congenital heart defects associated with Alagille syndrome. Development. 2012; 139(23): 4449-60.
32. Landskroner-Eiger S, Qiu C, Perrotta P, Siragusa M, Lee MY, Ulrich V, et al. Endothelial miR-17~92 cluster negatively regulates arteriogenesis via miRNA-19 repression of WNT signaling. Proc Natl Acad Sci U S A. 2015; 112(41): 12812-7.
33. Kivelä R, Bry M, Robciuc MR, Räsänen M, Taavitsainen M, Silvola JM, et al. VEGF-B-induced vascular growth leads to metabolic reprogramming and ischemia resistance in the heart. EMBO Mol Med. 2014; 6(3): 307-21.
34. Edwards D, Lewis J, Battle M, Lear R, Farrar G, Barnett DJ, et al. (99m)Tc-NC100668, a new tracer for imaging venous thromboemboli: pre-clinical biodistribution and incorporation into plasma clots in vivo and in vitro. Eur J Nucl Med Mol Imaging. 2006; 33(11): 1258-65.
35. Ichinose A. Factor XIII is a key molecule at the intersection of coagulation and fibrinolysis as well as inflammation and infection control. Int J Hematol. 2012; 95(4):362-70.
36. Heymann MA, Payne BD, Hoffman JI, Rudolph AM. Blood flow measurements with radionuclide-labeled particles. Prog Cardiovasc Dis. 1977; 20(1): 55-79.
37. Su H, Spinale FG, Dobrucki LW, Song J, Hua J, Sweterlitsch S, et al. Noninvasive targeted imaging of matrix metalloproteinase activation in a murine model of postinfarction remodeling. Circulation. 2005; 112(20): 3157-67.
38. Li S, Sinusas AJ, Dobrucki LW, Liu YH. New approach to quantification of molecularly targeted radiotracer uptake from hybrid cardiac SPECT/CT: methodology and validation. J Nucl Med. 2013; 54(12): 2175-81.
39. Mosseri M, Schaper J, Admon D, Hasin Y, Gotsman MS, Sapoznikov D, et al. Coronary capillaries in patients with congestive cardiomyopathy or angina pectoris with patent main coronary arteries - ultrastructural morphometry of endomyocardial biopsy samples. Circulation. 1991; 84: 203-210.
40. Robinson BR, Houng AK, Reed GL. Catalytic life of activated factor XIII in thrombi. Implications for fibrinolytic resistance and thrombus aging. Circulation. 2000; 102:1151-1157.
41. Shaw LJ, Bairey Merz CN, Pepine CJ, Reis SE, Bittner V, et al. Insights from the NHLBI-Sponsored Women's Ischemia Syndrome Evaluation (WISE) Study: Part I: gender differences in traditional and novel risk factors, symptom evaluation, and gender-optimized diagnostic strategies. J Am Coll Cardiol. 2006; 47(3 Suppl): S4-S20.
42. Zorach B, Shaw PW, Bourque J, Kuruvilla S, Balfour PC Jr, Yang Y, et al. Quantitative cardiovascular magnetic resonance perfusion imaging identifies reduced flow reserve in microvascular coronary artery disease. J Cardiovasc Magn Reson. 2018; 20(1): 14.
43. Campisi R, Marengo FD. Coronary microvascular dysfunction in women with nonobstructive ischemic heart disease as assessed by positron emission tomography. Cardiovasc Diagn Ther. 2017; 7(2): 196-205.
44. Nahrendorf M, Aikawa E, Figueiredo JL, Stangenberg L, van den Borne SW, Blankesteijn WM, et al. Transglutaminase activity in acute infarcts predicts healing outcome and left ventricular remodelling: implications for FXIII therapy and antithrombin use in myocardial infarction. Eur Heart J. 2008; 29(4): 445-54.
45. Jaffer FA, Tung CH, Wykrzykowska JJ, Ho NH, Houng AK, Reed GL, et al. Molecular imaging of factor XIIIa activity in thrombosis using a novel, near-infrared fluorescent contrast agent that covalently links to thrombi. Circulation. 2004; 110(2): 170-6.
46. Kaski JC, Aldama G, Cosín-Sales J. Cardiac syndrome X. Diagnosis, pathogenesis and management. Am J Cardiovasc Drugs. 2004; 4(3): 179-94.
47. Versari D, Daghini E, Virdis A, Ghiadoni L, Taddei S. Endothelial Dysfunction as a Target for Prevention of Cardiovascular Disease. Diabetes Care. 2009; 32 Suppl 2: S314-21.
48. Suzuki H, Takeyama Y, Koba S, Suwa Y, Katagiri T. Small vessel pathology and coronary hemodynamics in patients with microvascular angina. Int J Cardiol. 1994; 43: 139-50.

49. Silvain J, Collet JP, Nagaswami C, Beygui F, Edmondson KE, Bellemain-Appaix A, et al. Composition of coronary thrombus in acute myocardial infarction. J Am Coll Cardiol. 2011; 57(12): 1359-67.
50. Falati S, Gross P, Merrill-Skoloff G, Furie BC, Furie B. Real-time in vivo imaging of platelets, tissue factor and fibrin during arterial thrombus formation in the mouse. Nat Med. 2002; 8(10): 1175-81.